Check for updates

Research Paper

EARTHQUAKE SPECTRA

Earthquake Spectra
1–28
© The Author(s) 2023
Article reuse guidelines:
sagepub.com/journals-permissions
DOI: 10.1177/87552930231206399
journals.sagepub.com/home/eqs
Sage

Bayesian analysis of ground motion models using chimney fragility curves: 2021, 5.9-Mw Woods Point intraplate earthquake, Victoria, Australia

James La Greca[1], Mark Quigley[1], Jaroslav Vaculik[2], Peter Rayner[1], and Trevor Allen[3]

Abstract

The 22 September 2021 (AEST) M_W 5.9 Woods Point earthquake occurred in an intraplate setting (southeast Australia) approximately 130 km East Northeast of the central business district of Melbourne (pop. ~5.15 million). A lack of seismic instrumentation and a low population density in the epicentral region resulted in a dearth of near-source instrumental and "felt" report intensity data, limiting evaluation of the near-source performance of ground motion models (GMMs). To address this challenge, we first surveyed unreinforced masonry chimneys following the earthquake to establish damage states and develop fragility curves. Using Bayesian inference, and including pre-earthquake GMM weightings as Bayesian priors, we evaluate the relative performance of GMMs in predicting chimney observations for different fragility functions and seismic velocity profiles. At the most likely V_{S30} (760 m/s), the best performing models are AB06, A12, and CY08SWISS. GMMs that were preferentially selected for utility in the Australian National Seismic Hazard Model (NSHA18) prior to the Woods Point earthquake outperform other GMMs. The recently developed NGA-East GMM performs relatively well in the more distal region (e.g. >50 km) but is among the poorest performing GMMs in the near-source region across the range of V_{S30}. Our new method of combining analysis of engineered features (chimneys) with Bayesian inference to evaluate the near-source performance of GMMs may have applicability in diverse settings worldwide, particularly in areas of sparse seismic instrumentation.

[1]School of Geography, Earth, and Atmospheric Sciences, The University of Melbourne, Parkville, VIC, Australia
[2]School of Civil, Environmental and Mining Engineering, The University of Adelaide, Adelaide, SA, Australia
[3]Community Safety Branch, Geoscience Australia, Canberra, ACT, Australia

Corresponding author:
James La Greca, School of Geography, Earth and Atmospheric Sciences, The University of Melbourne, Parkville, VIC 3053, Australia.
Email: jlagreca@student.unimelb.edu.au

Keywords
Earthquake hazard, ground motion models, fragility curve, chimney, Bayesian

Date received: 20 October 2022; accepted: 11 September 2023

Introduction

Ground-motion models (GMMs) are a key component of probabilistic seismic hazard analysis (PSHA) (Bommer et al., 2010). In stable continental regions (SCRs) where moderate-to-large earthquakes are infrequent and the spatial density of seismic networks may be low, instrumental strong ground motion data can be rare, particularly in near-source areas (e.g. 0–50 km epicentral distances). This can compromise objective analysis of GMM parameters and performance in forecasting ground shaking intensities and distributions (Leonard et al., 2014).

In Australia, development of the National Seismic Hazard Assessment (NSHA) is led by Geoscience Australia (GA). The NSHA 2018 (Allen et al., 2018) used an expert elicitation process to select and weight GMMs used to develop the seismic hazard model (Griffin et al., 2018, 2020). An important aspect of selecting and ranking GMMs for use in hazard assessments is the comparison of instrumentally recorded ground motions with theoretical outputs from the GMMs (e.g. Ghasemi and Allen, 2018). The development of Australian-specific GMMs is a challenging task given the sparse recording networks and limited strong-ground-motion recordings. Three GMMs that have been specifically developed for the region are commonly used in Australian seismic hazard assessments: A12 (Allen, 2012), SEA09YC (Somerville et al., 2009—Yilgarn craton), and SEA09NC (Somerville et al., 2009—non-cratonic). Other models used in NSHA 2018 have been adapted from California (BEA14; Boore et al., 2014), Europe (CY08SWISS; Edwards et al. 2016 and CY14; Chiou and Youngs, 2014), and Central Eastern US (AB06; Atkinson and Boore, 2006). In previous versions of the NSHA, two other GMMs curated for Australia were used as candidates: Gea90SEA (Gaull et al., 1990—South-East Australia) and Gea90WA (Gaull et al., 1990—Western Australia. Gea90SEA and WA GMMs were not used in the 2012 (Leonard et al., 2014) or 2018 (Allen et al., 2018) NSHAs, as these GMMs were calibrated to local magnitude (M_L) and were developed based on the attenuation of macroseismic intensities. Future revisions of the NSHA are considering the adoption of the Next Generation Attenuation for Central and Eastern North America (NGA-East; Goulet et al., 2021) as a GMM candidate. For the purposes of this article, the "NGA-East" model refers to the weighted mean GMM from an ensemble of GMMs (Goulet et al., 2021) that we adjust from the reference site condition of $V_{S30} = 3000$ m/s to a range of V_{S30} values from 270 to 1100 m/s to account for the possible site conditions discussed herein. GMM constant terms and parameter uncertainties associated with V_{S30} scaling represent sources of epistemic uncertainty (Ramos-Sepulveda et al., 2022) that we cannot resolve in this study.

Recently, Hoult et al. (2021a, 2021b) evaluated several GMMs in comparison to the ground motion recordings of the 2012 5.1 M_W Moe and 2021 Woods Point earthquakes in Victoria, Australia (Figure 1). For the Moe earthquake, there was a tendency for all GMMs to over-predict near-source (within a rupture distance of 40 km) ground motions; this was particularly the case for the mean NGA-East GMM (Goulet et al., 2017). Hoult et al. (2021b) concluded that AB06 and A12 perform well, at smaller epicentral distances (<70–100 km but >40 km) and particularly at shorter spectral periods. For the Woods

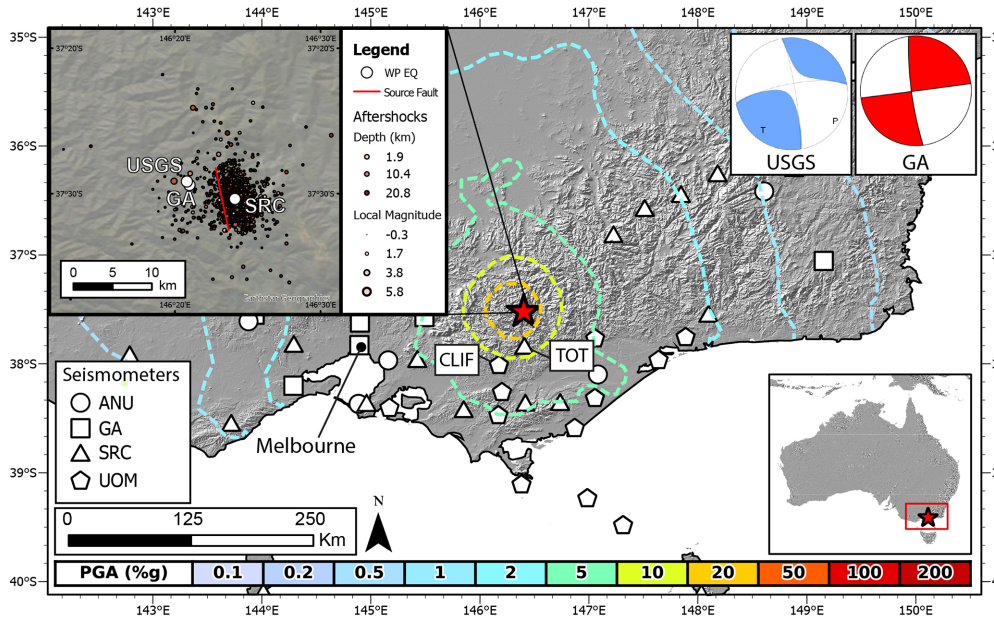

Figure 1. Map of seismometer locations in southeastern Victoria and Geoscience Australia's ShakeMap contours for PGA (https://earthquakes.ga.gov.au/event/ga2021sqogij). The seismometers legend refers to the organization operating and maintaining the seismometer. Two focal mechanisms are presented from USGS and GA. The USGS solution for nodal plane (NP) 1 is a strike of 259°, dip of 75°, and rake of 174°. The USGS solution for NP2 is a strike of 351°, dip of 84°, and a rake of 15°. The GA solution for NP1 is a strike of 172°, dip of 83°, and rake of 0°. The GA solution for NP2 is a strike of 82°, dip of 90°, and rake of 173°. Inset map displays Woods Point earthquake aftershocks located by the Seismology Research Centre relative to the projected source fault and main shock epicenter locations from GA, USGS and SRC.
ANU: Australian National University; GA: Geoscience Australia; SRC: The Seismology Research Center; UOM: The University of Melbourne

Point earthquake, the absence of recorded ground motions at distances less than ~60 km from the rupture precluded the evaluation of near-source GMM performance. Several GMMs (NGA-East, AB06, A12, Sea09) performed well at >60 km distances (Hoult et al., 2021b), with some variability in performance at different periods. At larger rupture distances (i.e. >100 km), GMMs that incorporate an attenuation "transition zone" due to the strong postcritical reflections from the Moho discontinuity (Allen et al., 2007; Atkinson, 2004) tended to provide better fits to the data at mid-to-longer spectral periods (e.g. AB06, A12, and NGA-East) (see Figure 2). This was also the case for the Moe earthquake (Hoult et al., 2021a). Hoult et al. (2021a, 2021b) emphasized the need to further evaluate GMMs to assist in logic tree weightings in PSHAs; we pursue this in this study.

Unreinforced masonry (URM) chimneys are among the most damage-prone components across any building class when subjected to earthquake ground motion (Krawinkler et al., 2012; Maison and McDonald, 2018; Moon et al., 2014). The natural period range of chimneys in 1–3 story buildings is 0.05–0.2 s. This period range falls within the typical high acceleration region of the design response spectrum (Klopp, 1996—see Chapter 3 therein); Maison and McDonald (2018) use a standard natural frequency of the host

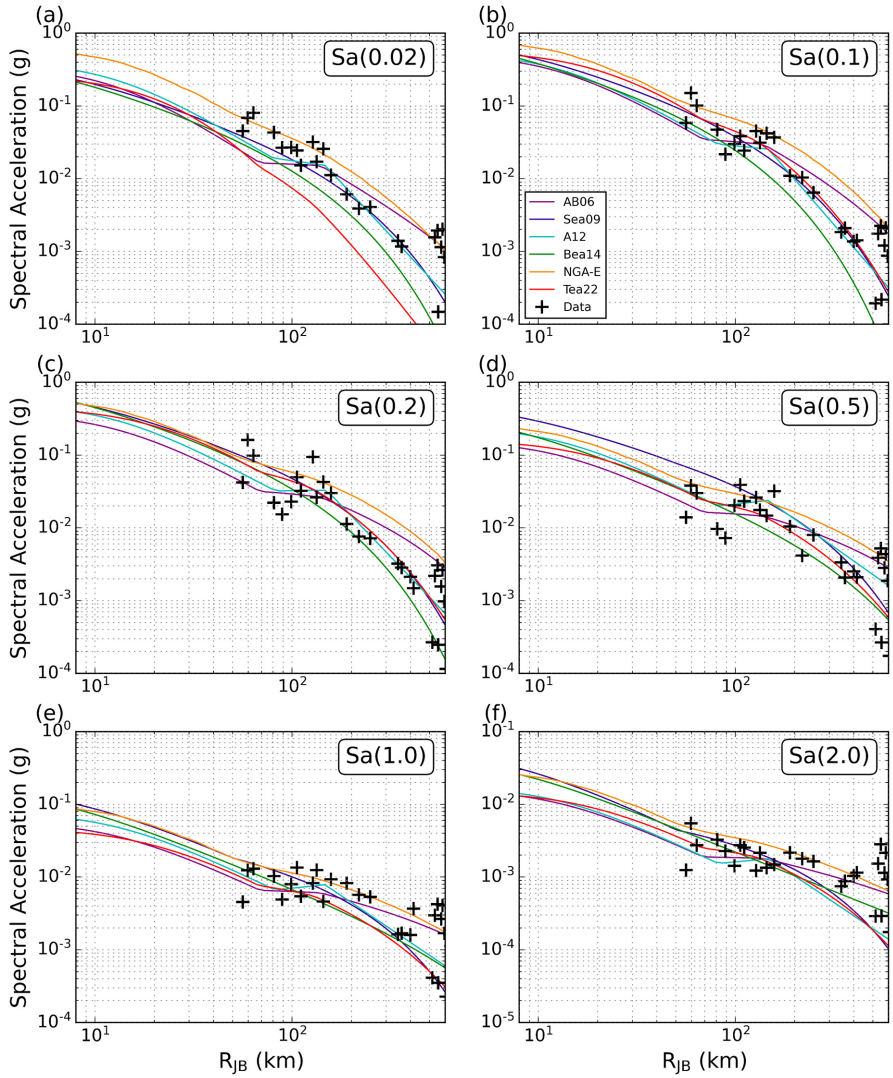

Figure 2. Spectral accelerations recorded for the 5.9 MW, 22 September 2021 (AEST) Woods Point earthquake plotted relative to GMMs considered applicable for southeastern Australia. There are six subplots for differing periods: (a) T=0.02, (b) T=0.1, (c) T=0.2, (d) T=0.5, (e) T=1.0, and (f) T=2.0 s. GMM acronyms: AB06 = Atkinson and Boore (2006), Sea09 = Somerville et al. (2009) for non-cratonic sources, A12 = Allen (2012), Bea14 = Boore et al. (2014), CY14 = Chiou and Youngs (2014), Tea19 = Tang et al. (2022), and NGA-E = Next Generation Attenuation East, Goulet et al. (2017). The GMMs are plotted for a reference site condition with a VS30 of 760 m/s. RJB is the Joyner-Boore distance which represents the shortest distance of a site to the surface projection of the fault plane.

structure (i.e. house) of 6 Hz (0.16 s). Modeling of masonry chimney fragility curves can provide a prediction of seismic vulnerability and damage in the event of an earthquake as an expression of peak ground accelerations (PGAs) within a range of frequencies. This article presents a novel approach of using chimney damage states and their respective fragility curves to approximate earthquake shaking intensities using Bayesian techniques. Fragility curves define a cumulative distribution function with respect to a ground-motion

intensity measure, commonly PGA. The intersection between the fragility curve and the output of a GMM defines the probability of damage (Heresi and Miranda, 2021; Maison and McDonald, 2018). In this study we use Bayesian modeling to evaluate the relative performance of GMMs based on their modeled PGA outputs relative to calculated PGA ranges from observations of chimney damage (or lack thereof) and associated chimney fragility curves.

Bayes' theorem (Bayes, 1764; Joyce, 2003) states that one can calculate the posterior probability using a prior probability and likelihood function. If the likelihood of a calculated PGA (derived from a GMM) to cause damage to a chimney is known, the likelihood a GMM correctly predicts the observation can be calculated. Therefore, using Bayes theorem and residential chimney fragility functions, the likelihood that a GMM represents the expected damage outcome of a set of chimneys after an earthquake can be deduced.

This article aims to answer the following questions:

1. Using earthquake damage of chimneys and their respective fragility curves as a proxy for seismic ground motions at near-source locations, what is the relative performance of commonly used GMMs in terms of their ability to predict the chimney damage observations?
2. How do the relative weightings of GMMs established from a chimney analysis using a Bayesian approach compare with pre-Woods Point earthquake NSHA18 weightings of GMMs?

This article outlines a method to evaluate the relative performance of GMMs in an earthquake using proxy indictors (chimneys) to compensate for an absence of near-source instrumental seismological data. Two chimney fragility curve models (Model 1: Maison and McDonald, 2018; Model 2: Vaculik and Griffith, 2019) and median GMM PGA curves are used as inputs into a Bayesian analysis. The Bayesian approach is used to determine which GMM best predicts chimney damage/non-damage observations from the Woods Point earthquake.

2021 M_W 5.9 Woods Point earthquake

At 9:15 am on 22 September 2021 (AEST), a moment magnitude (M_W) 5.9 earthquake occurred in southeast Australia within the Southeast Seismic Zone, approximately 130 km ENE of Melbourne's CBD (Figure 1). This intraplate event was the largest earthquake in the state of Victoria since European record keeping began in the early 1800s (McCue, 2015). The epicentral region is sparsely populated; Woods Point (pop. 33), Jamieson (pop. 382), and Licola (pop. 11) (see Figure 4) are the three settlements nearest the epicenter (2021 Census). The mainshock occurred in the Victorian Highlands, approximately 13 km ENE from Woods Point. Four epicentral locations have been published (Table 1).

Table 1. Woods Point earthquake epicenter locations as reported by varying institutions

Institution	Latitude	Longitude	Depth (km)
Geoscience Australia (GA)	−37.490	146.350	10
Seismology Research Center (SRC)	−37.506	146.402	12.7
United States Geological Survey (USGS)	−37.486	146.347	12 (±1.7)
Mousavi et al. (2023)	−37.500	146.390	16.8

The location published by SRC is preferred as it uses additional data from industry and university seismic networks that are not used in the GA and USGS solutions. The north–south trending aftershock distribution (Figure 1) coupled with mainshock focal mechanism solutions suggests a steeply west dipping (83°; strike 172°) (GA) to steeply east dipping (84°; strike 351°) (USGS) left-lateral strike-slip source fault mechanism (Figure 1). SRC aftershock data were fit by linear interpolation in map view and cross-section to delineate an ~8 km long, 9 km down-dip NNW-striking mainshock rupture plane with ~85°E dip (Quigley et al., 2021; Quigley and La Greca, 2021). This rupture-source model is generally consistent with focal mechanism constraints and is used for the analyses herein. The nearest seismometer is a short period passive sensor, located 35 km from the epicenter at Thompson Reservoir (TOT) (Figure 1). Earthquake waveforms at TOT clipped under the Woods Point earthquake ground motions. Preliminary observations of ground motions (Hoult et al., 2021b) omit TOT data from analysis.

Geoscience Australia used four equally weighted GMMs (Atkinson and Boore, 2006 (AB06), Somerville et al., 2009 non-cratonic (Sea09NC), Allen, 2012 (A12), and Boore et al., 2014 (Bea14)) and a 0–30 m depth-time averaged shear-wave velocity model (V_{S30}) based on the Australian Seismic Site Conditions Map (McPherson, 2017) to produce PGA contour plots for the Woods Point earthquake (Figure 1) (e.g. Allen et al., 2019, 2023). These PGA contours are informed by the "ShakeMap" system in which GMMs, ground motion amplification (McPherson, 2007), and felt reports are combined to create a map of seismic intensity (Allen et al., 2019; Wald et al., 2010). Estimated PGAs within the epicentral region are ~0.2 g. Calculated PGAs in Melbourne based on Geoscience Australia's ShakeMap range from 0.02 to 0.05 g (Figure 1).)

Instrumentally recorded spectral accelerations (SAs) of the Woods Point earthquake are primarily within the range of the suite of median values predicted by GMMs at diverse periods and distances (Figure 2). The performance of GMMs at individual sites is challenging to evaluate because local V_{S30} estimates are poorly constrained, and potential variations in V_{S30} provide a source of epistemic uncertainty in evaluating GMM performance. Consequently, adherence to the assumed reference site condition of $V_{S30} = 760$ m/s that is used to model the GMMs in Figure 2 and Hoult et al. (2021b) is uncertain; it is possible that inclusion of site-specific V_{S30} data could affect the relative performance of GMMs (this is beyond the scope of this study but is a topic of ongoing research). SAs in excess of GMM estimates across the range of periods and source distances (Figure 2) could also reflect source effects associated with specific characteristics of the Woods Point earthquake (e.g. radiation effects, high source energy release, faulting mechanism, source geometry, path effects, and/or site effects such as amplification associated with low V_{S30} host materials and basin effects) that may be distinct from the "average" observations from reference earthquakes used in GMM generation. Hoult et al. (2021b) show that short period ($T < 0.1$) SAs appear to be best matched by central and/or northeast American developed GMMs (NGA-East and AB06), while models developed for southeast Australia such as A12 "predict the attenuation, particularly at lower frequencies." The absence of observational data at epicentral distances <60 km precludes comparison of GMM predictions against observations in the near-source region.

Modified Mercalli intensity (MMI) data derived from more than 43,000 "felt" reports range from MMI VIII to MMI I (Figure 3). Felt reports were submitted from epicentral distances ranging from <20 to >700 km (Figure 3a). Very few (<10) felt reports were submitted from the near-source region (<50 km) and there is large variability in MMI reports within "binned" epicentral distances (e.g. 40 km distance; Figure 3b), reflected by

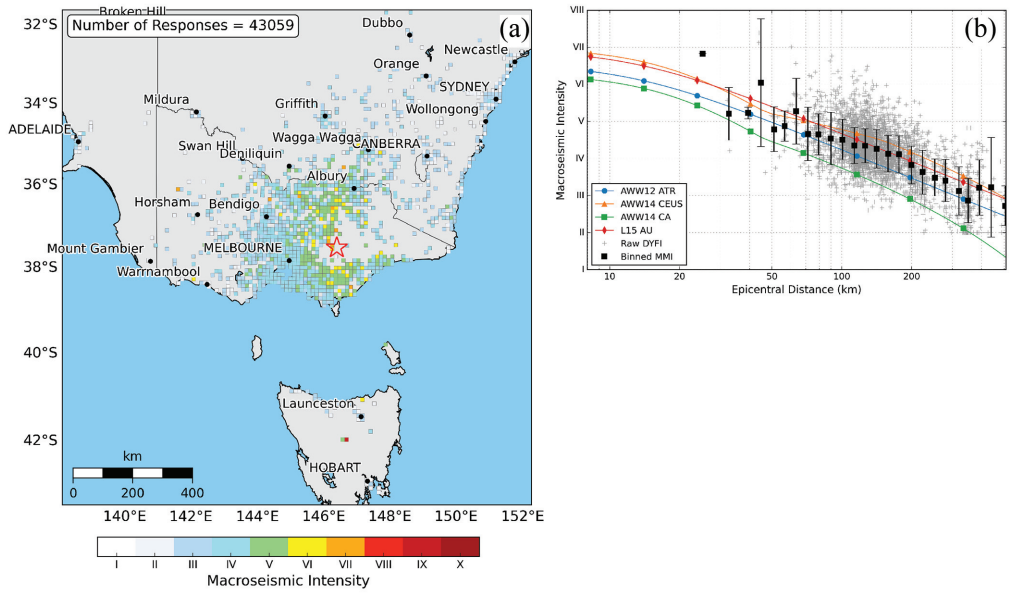

Figure 3. (a) "Felt" grid estimated from >43,000 "felt" reports submitted to Geoscience Australia following the 22 September 2021 Woods Point earthquake. (b) MMI attenuation model equations of the 5.9-Mw Woods Point earthquake with 1σ confidence using MMI GMMs. Mean Binned MMI are spaced at 0.1 $\log_{10}$ kms. GMM acronym: AWW12 ATR = Allen et al. (2012); AWW14 CEUS = Atkinson et al. (2014)—Central Eastern US; AWW14 CA = Atkinson et al. (2014)—California; L15—Leonard (2015).

standard deviations (1σ) about the mean of >1 to 2 MMI increments. Mean MMIs generally decrease with increasing epicentral distance. Mean MMIs adhere most closely to the Australia-based (L15 AU) and eastern US-based (AWW14 CEUS) MMI versus distance intensity prediction models; AWW12 ATR (active crustal region) and AWW14 CA (California) models tend to underpredict observed MMIs (Figure 3b). At equivalent epicentral distances, MMIs tend to be higher northern and southern quadrants relative to eastern and western quadrants, although data are limited due to sparse population in the east. The dense urban population of Melbourne results in a sampling distribution biased into the western quadrant at 100–150 km epicentral distances. The dearth of near-source MMIs further illustrates the challenge of understanding near-source shaking intensities in this earthquake and highlights the need for consideration of other shaking intensity proxies.

Woods Point reconnaissance survey

A reconnaissance field survey of environmental and infrastructure damage in the epicentral area commenced ~30 h after the earthquake (23–27 September 2021) (La Greca and Quigley, 2021; Quigley and La Greca, 2021). Subsequent field surveys were undertaken on 8–10 and 23–26 October. We identified 43 brick masonry and four stone chimneys (n = 47), including chimneys with observational evidence for damage (Figure 4). All chimneys were physically examined, precisely located, and photographed from multiple angles (Figure 5). Chimney width and heights were determined by brick counting on photographic images, using the average Australian brick size (76 mm high × 230 mm long ×

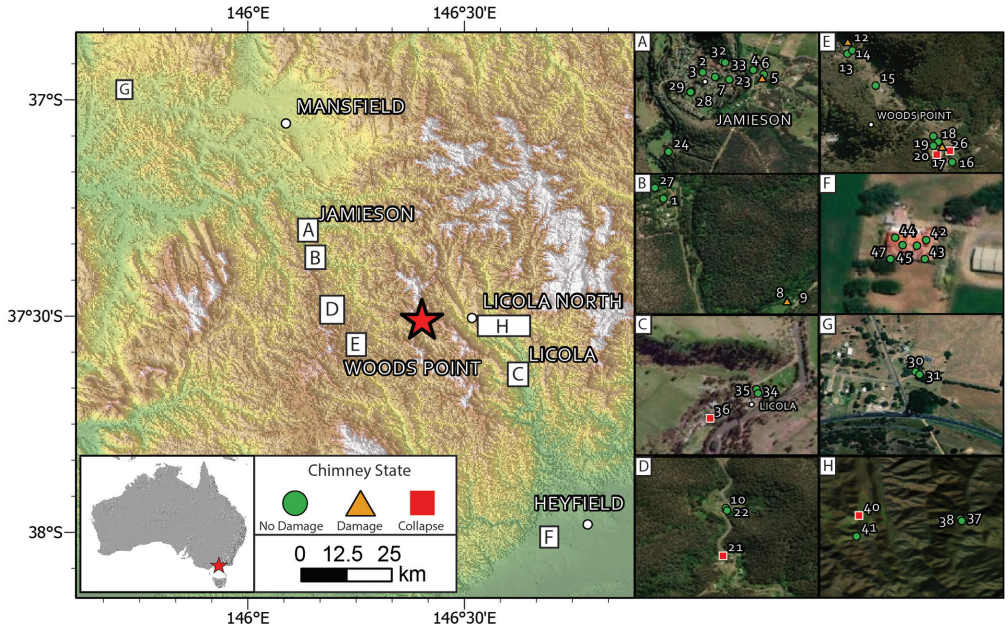

Figure 4. Map of chimneys observed in the reconnaissance survey and their respective collapse state resultant from the Woods Point earthquake.

Figure 5. Photographs of chimneys with various damage states post the Woods Point earthquake.

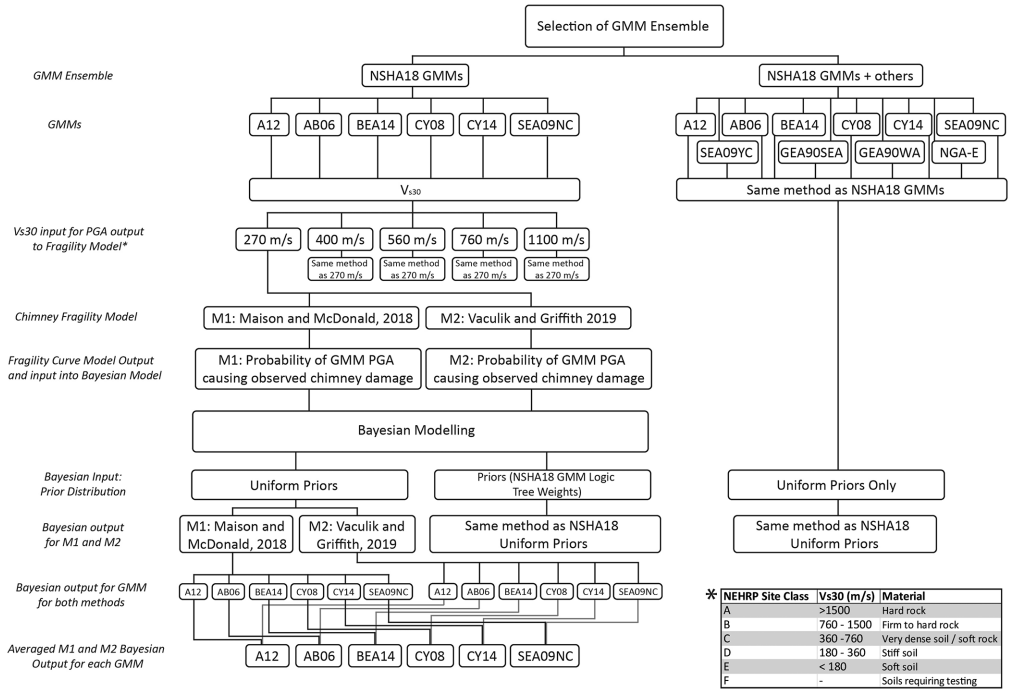

Figure 6. Summary of methodology.

110 mm wide), with exception of the four stone chimneys, where height was approximated using scaled photographs. Visual inspection of mortar in the field and in photographs enabled us to estimate mortar "quality" and "age." This included up close investigation of the mortar, determining whether it was flaking and/or breaking apart. Mortar rankings from "Weak" to "Expected" were assigned to each chimney and entered as a data input in relevant fragility analyses (see *fragility curve methods* below). Mortar observations also enabled us to distinguish earthquake from pre-earthquake damage; for example, if a chimney had small cracking in the mortar and/or bricks but had moss growing within the crack, it was interpreted to be pre-seismic deformation. All chimney data are presented in Supplemental Appendices A and B. Of the total chimneys observed, five were determined to have collapsed in the earthquake or suffered extensive damage.

Methodology

Selection of GMMs

A schematic of the methodology is provided in Figure 6. The GMMs analyzed in this study are those used in the Australian NSHA18 and predecessor NSHAs, or are considered as candidate GMMs for future NSHAs (Table 2). The respective expert elicitation weights for NSHA18 GMMs are shown in Table 2.

URM chimney fragility models

The vulnerability of URM chimneys to earthquake ground motions was modeled using the fragility models of Maison and McDonald (2018) and Vaculik and Griffith (2019). The

Table 2. Final GMM weights applied in the NSHA18, modified from the ground-motion characterization expert elicitation workshop (adapted from Table 8 in Griffin et al., 2018)

Model name	GMM weighting	Reference
Allen2012 (A12)	0.208	Allen (2012)
AtkinsonBoore2006 (AB06)	0.138	Atkinson and Boore (2006)
BooreEtAl2014 (BEA14)	0.166	Boore et al. (2014)
ChiouYoungs2008SWISS01 (CY08SWISS)	0.153	Edwards et al. (2016)
ChiouYoungs2014 (CY14)	0.130	Chiou and Youngs (2014)
SomervilleEtAl2009NonCratonic (SEA09NC)	0.205	Somerville et al. (2009)

GMM: ground motion model.

output of both models is a set of analytical fragility curves that express the probability of a chimney reaching a particular damage state as a function of ground motion intensity in terms of the PGA. Increasing chimney resilience shifts fragility curves toward higher PGA values. These curves in turn serve as the input into the Bayesian analysis in the subsequent portion of this article. The decision to consider two separate fragility models was made to improve the reliability of the Bayesian inference process given the inherent uncertainty in relating the expected damage states to ground motion intensity. PGA values are calculated using selected GMMs within the OpenQuake *hazardlib* software library at a distance equivalent to the source-to-site distance required by the GMM for each chimney on a range of site conditions (Pagani et al., 2014). These estimates were used to determine the probability of the chimney sustaining the degree of damage (or non-damage) that was observed. The Bayesian analysis represents the likelihood of each individual GMM to correctly predict the field-derived damage observations under the assumption that the fragility curve is representative of a chimney's damage potential. In addition, the Bayesian analysis considers and incorporates two prior inputs. A uniform prior which assumes that all GMMs have an equal weight before entering the Bayesian analysis and an NSHA18 prior approach, where the NSHA18 logic tree weights are applied into the Bayesian analysis. PGA values output by GMMs in this process do not consider aleatory variability and assumes that the median GMM value is the PGA at the site of the chimney.

Fragility curve Model 1 (M1)

The fragility curves of Maison and McDonald (2018) were determined using a single-degree-of-freedom computer model (Maison and McDonald, 2018). Fragility curves incorporate the effects of various site parameters including chimney height above roof, masonry flexural tensile strength, chimney section dimensions, vertical steel reinforcement, and chimney-house anchorage strength. Damage functions for URM chimneys are expressed as a function of PGA, chimney height, and expected masonry tensile strength for the chimneys part of this study can be seen in Figure 7a and b.

A select set of chimneys in the Woods Point epicentral region did not meet the brick base templates used in Maison and McDonald (2018). Maison and McDonald (2018) suggest that the shortest measurement of either the length or width of the chimney dictates the damage function (Figure 8). Therefore, in this study for a chimney to be included it must meet only one measurement of the brick base outlined in Figure 7a and b.

Model 1 cannot be used for all chimneys due to non-adherence of chimney characteristics, including chimney brick type (stone chimneys were omitted), height, and brick base,

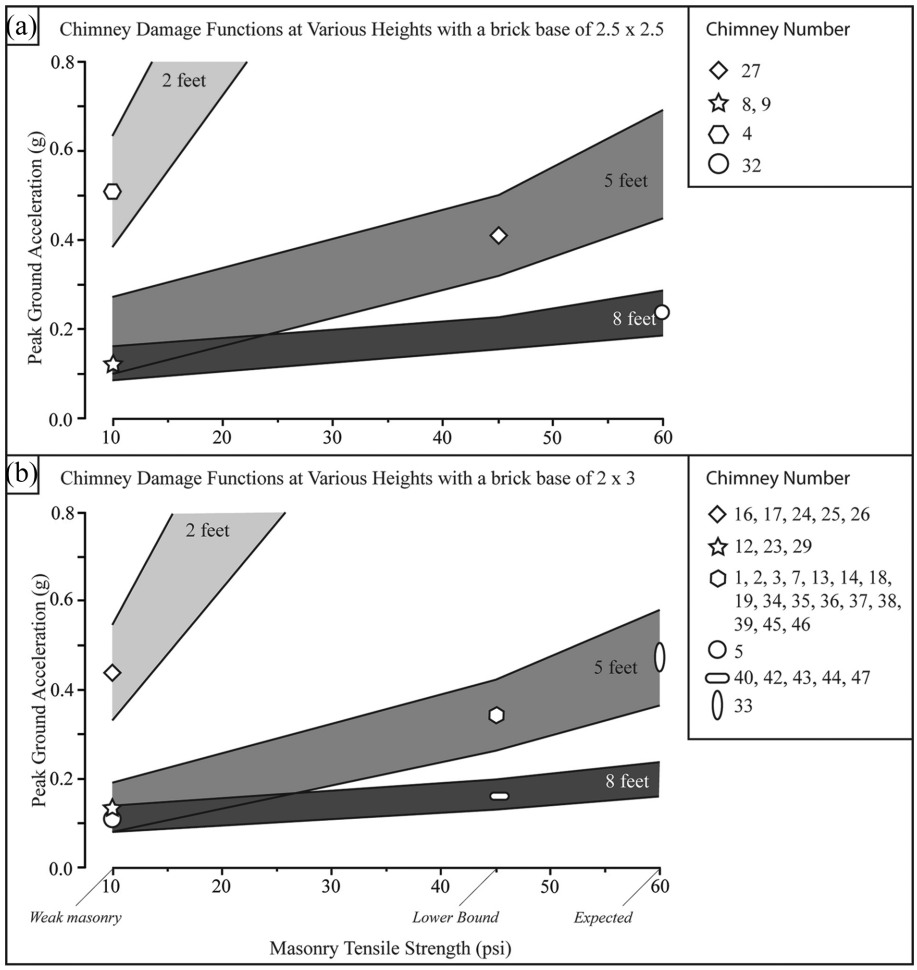

Figure 7. Damage functions for chimneys as outlined by Maison and McDonald (2018) with (a) chimneys with a brick base of 2.5 x 2.5, and (b) chimneys with a brick base of 3 x 3. Chimneys from the reconnaissance survey plotted onto the damage curve to obtain median value. The shaded region represents 50% chances of suffering extensive damage. The median value of fragility function has been correlated to the respective chimneys.

to the parameters in the regressions (Figure 7); chimneys 6, 10, 11, 15, 20, 21, 22, 30, 31, and 41 were excluded from analysis. All chimneys are evaluated using Model 2 (see next section).

The damage function defines a PGA range of 50% probability of failure for varying tensile strengths and chimney brick base (Figure 7). To enable a range of values to be represented by a single value in fragility curve analyses, we extract the median PGA value of the 50% PGA range in the damage functions. We identify this as a model simplification as we do not consider the full range of the 50% chance of failure field. Following Maison and McDonald (2018), we use a beta value of 0.6 as per US FEMA P-58 Seismic Performance Assessment of Buildings, Methodology, and Implementation guidelines (Federal Emergency Management Agency (FEMA), 2018).

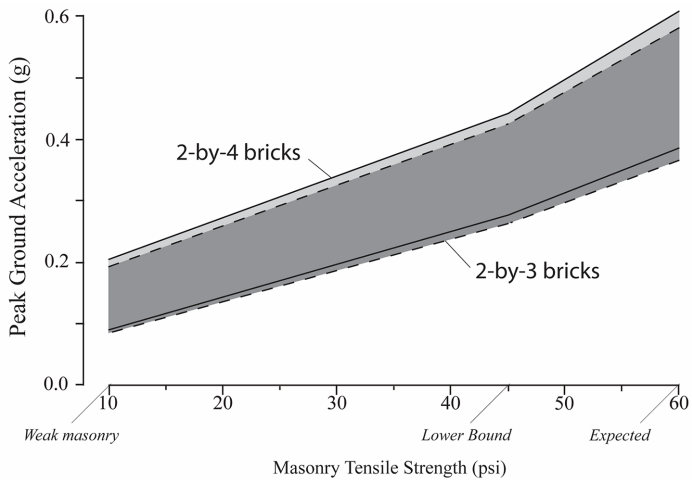

Figure 8. Damage functions for plan chimneys of 5-ft height with different brick base showing section width has negligible effect (Maison and McDonald, 2018).

Fragility curve Model 2 (M2)

Model 2 follows the analytical two-step time-history analysis (THA) approach described in Vaculik and Griffith (2019). We first perform a THA on the parent building with excitation by the ground motion to compute the motion at the top of the building. This motion is then used to undertake a nonlinear THA of the chimney. The chimney's force–displacement behavior was defined using a bilinear rule with a descending post-yield branch to represent rocking behavior (Vaculik and Griffith, 2017). Unlike the Maison and McDonald approach, this model ignores any bond strength and assumes that the chimney's lateral load resistance is provided entirely from stabilization due to gravity. The force–displacement capacity of each chimney was constructed as a function of its geometry; that is, the height above the roof line and base width. In the case of rectangular chimneys (with unequal base widths), the shorter dimension was used. A factor of 0.9 was applied to the gross width of the chimney to account for deviation from idealized rigid behavior, for example, due to geometric imperfections and finite compressive strength.

Following the approach described in Vaculik and Griffith (2019), a set of five displacement-based damage levels were defined, ranging from D1 (first onset of cracking) to D5 (complete collapse). In order to align these with the observable damage levels in the field survey, these were condensed into three states: (1) no visible damage (damage $<$ D2), (2) visibly damaged but not collapsed (damage $\geqslant$ D2 and $\leqslant$ D4), and (3) collapsed (damage $>$ D4). Note that the onset of observable damage was set at D2 rather than D1, due to micro-cracking not being able to be visually assessed in the field.

This overall procedure was implemented within an incremental dynamic analysis (Vamvatsikos and Cornell, 2002) using a suite of code-compatible (Standards Australia, 2018) ground motions. The median PGAs to reach different damage states were computed, thus resulting in a standalone set of fragility curves for each chimney. Further detail regarding the overall approach can be found in Vaculik and Griffith (2019).

As with the first model, a beta value of 0.6 was adopted for the dispersion of the fragility curves consistent with FEMA guidelines.

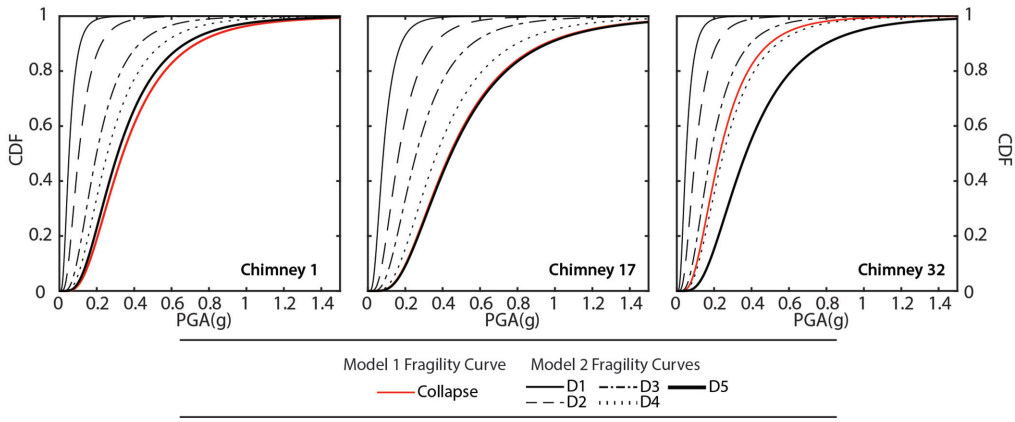

Figure 9. Examples of fragility curves from three different chimneys for both models of curve generation.

Plotting of fragility curves

Fragility curves were formulated in terms of the lognormal distribution, whose cumulative distribution function (CDF) can be expressed as:

$$F(x) = \Phi\left(\frac{lnx - \mu}{\beta}\right) \tag{1}$$

where x is the PGA; Φ is the standard normal CDF operator; μ is the natural logarithm of the median PGA at each damage state; and β is the coefficient of variation (Lallemant et al., 2015), which was taken as 0.6 in both models.

Illustrative examples of fragility curves obtained using the respective models are shown in Figure 9 (see Supplemental Appendix A for all chimneys). These consider three chimneys:

- Chimney 17—a stocky (~2 ft tall) chimney assumed to have weak bond (10 psi)
- Chimney 1—a medium-slenderness (~5 ft tall) chimney assumed to have typical-strength bond (60 psi)
- Chimney 32—a slender (~8 ft) tall chimney assumed to have normal-strength bond (60 psi)

It is seen that the solitary curves for Model 1 coincide roughly with damage state D5 curve in Model 2; and thus, the median PGA of the D4 curves in Model 2 (delineating the collapse state in the implementation throughout this article) are typically lower than the PGAs predicted by Model 1.

PGA—OpenQuake

OpenQuake (https://platform.openquake.org/) hazardlib.gsim library was used to compute the expected PGAs at each chimney (Pagani et al., 2014). Chimney distances to the fault rupture were calculated and used as input into the GMMs called from the OpenQuake

Table 3. Rupture inputs required for OpenQuake earthquake rupture centered on the hypocenter

Woods Point earthquake OpenQuake inputs	
M_W	5.9
Rake	0
Hypocenter longitude	146.402
Hypocenter latitude	–37.506
Hypocenter depth	12.7 km
Rupture type	Simple fault rupture
Dip	85°
Upper seismogenic depth (km)	4
Lower seismogenic depth (km)	13
Fault geometry (earthquake rupture tips)	146.394, –37.5417 146.380, –37.470

hazardlib.gsim library. Table 3 displays the fault geometry and inputs for GMM calculation.

The calculated PGA value from each GMM for each chimney can then be compared with the respective fragility curves. Figure 10 shows an example of five chimneys displaying that the intersection point of the expected PGA and the fragility curve determines probability values inputs for the Bayesian model.

The PGA–fragility curve intersection point represents the probability the chimney will exceed a specified damage state at that PGA for each given GMM for six selected chimneys. Depending on the damage state of the chimney resulting from the earthquake, the probability of the observed can be determined through either taking the intersection CDF (if chimney had damage), or through subtracting the CDF from 1 (if the chimney had no damage). M1 (Maison and McDonald, 2018) uses a binary damage state for collapse or no collapse (red line in Figure 10). M2 (Vaculik and Griffith, 2019) uses five damage states to model chimney damage (black lines in Figure 10). For chimneys that had damage but did not collapse, the CDFs for the damage range were subtracted from one another. These probabilities of observed values were used as inputs in the Bayesian approach.

Bayesian model

Bayesian modeling is a statistical approach based on Bayes' theorem using prior knowledge to update a statistical model (Van de Schoot et al., 2021). A prior distribution (prior knowledge) can be informed by new observational data to establish a new posterior probability. Bayes' theorem states that one can calculate the posterior probability if the prior probability and the likelihood function is known. The approach used here calculates the relative probability of a GMM (A) correctly predicting "modeled" PGAs that are independently inferred from the chimney fragility curves and observed damage state of a chimney (B) as proxies for the "observed" PGAs at individual sites in the earthquake.

This can be expressed as:

$$P(A|B) = \frac{P(B|A) \cdot P(A)}{P(B)} \tag{2}$$

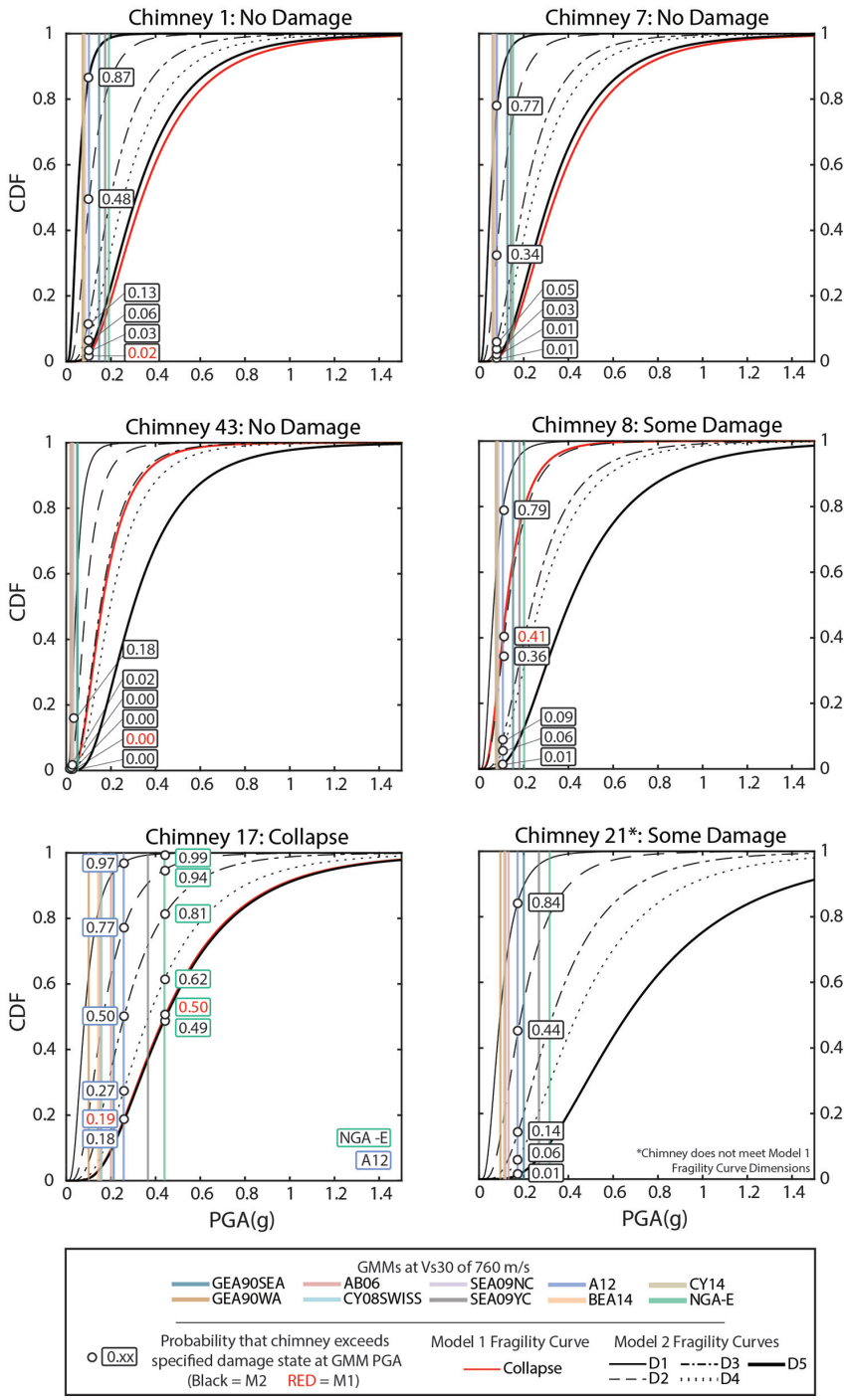

Figure 10. Selection of chimney fragility curves with the expected PGA for each GMM and the respective probability the chimney exceeds each damage state. The intersection points of GMM A12 with the fragility is highlighted and presents the probability that the PGA estimated by A12 would cause the defined fragility damage state. Chimney 17 also has NGA-East highlighted to show variation in GMM outputs.

Table 4. Outline of the definition of the probability of observed or P(B|A) for varying damage states for both fragility curve methods

Probability of observed for each method and damage state	M1	M2
Chimney collapsed	Probability of chimney collapse outlined in the M1 chimney fragility curve and respective GMM output.	Probability of chimney collapse outlined in Table 5 and respective GMM output.
Chimney damage	M1 does not account for chimney damage. Assumes the chimney is not damaged.	The probability of chimney damage is outlined in Table 5 and the respective GMM output.
No damage	The probability of the chimney not collapsing is outlined in M1 chimney fragility curve and respective GMM output.	Probability of chimney not collapsing or sustaining damage as outlined in Table 5 and respective GMM output.

GMM: ground motion model.

where P(A|B) is the probability a GMM is correct given event B (the posterior belief), P(B|A) is the probability of the observed chimney damage state given the GMM output; the probability of observed. Table 4 outlines the probability of observed for each method and damage type.

P(B) is the summed probability of each chimney to be damaged as outlined by their fragility curve for all GMM and P(A) is the prior distribution of our GMM before the earthquake event. P(B|A) is determined through three different equations depending on the state of the chimney. As there are two methods of fragility curve generation, this analysis will examine the combination of these methods into a singular P(B|A) value.

Calculation of P(B|A)

M1. There are two states of chimneys considered for Model 1; chimneys that have collapsed (P1), and chimneys that have not (P2). For chimneys that have collapsed, the fragility curve dictates the probability of the observed and therefore is represented as Equation 3:

$$P1 = p(B1_C|A) = \prod \Phi\left(\frac{lnx - \mu_{M1}}{\beta}\right) \tag{3}$$

For chimneys that have not collapsed, the probability is represented as the probability of not P1 (Equation 4):

$$P2 = p(B1_{NC}|A) = \prod 1 - \Phi\left(\frac{lnx - \mu_{M1}}{\beta}\right) \tag{4}$$

where x = specified PGA value for individual chimney with subscript highlighting M1
μ = Natural Log value of fragility curve median
β = beta value in fragility curve analysis
Φ is the standard normal CDF operator
$B1 = \{set\ of\ collapsed\ chimneys\ that\ can\ be\ modeled\ by\ Fragility\ Model\ 1\ (M1)\}$
$B1_C = \{subset\ of\ chimneys\ from\ B1\ that\ collapsed\}$
$B1_{NC} = \{subset\ of\ chimneys\ from\ B1\ that\ did\ not\ collapse\}$

The probability of observed for a GMM for fragility model 1 ($P_{observed(M1)}$) can be calculated as the product of P1 and P2:

$$P_{observed(M1)} = p(B1|A_{GMM}) = P1 * P2 \tag{5}$$

M2. Model 2 considers three damage states: undamaged, damaged, and collapse (Table 5). These are characterized by five damage levels (D-Levels) in which Table 5 outlines the relationship between the fragility curve D-Level and observed damage state of a respective chimney. Therefore, to calculate the P(B|A) for a GMM that incorporates three chimney damage states, three equations are derived. The undamaged state is represented in Equation 6. "No damage" is interpreted as not exceeding a D-Level of 2, and therefore the median value (μ) is defined by the D2 curves in Supplemental Appendix C for each chimney. Equation 7 is for chimneys that have sustained damage, but not total collapse. This is the probability the chimney would sustain a lower damage level, then subtracting the probability the chimney would fail from the higher damage level. This assumes a level of damage greater than a D-Level of 2 but not greater than 4. Equation 8 is for chimneys that have failed and therefore exceed a D-Level of 4. These three calculations state the probability of the observed event and can be seen in Supplemental Appendix D:

$$P3 = p(B2_{NC}|A) = \prod 1 - \Phi\left(\frac{lnx - \mu_{D2}}{\beta}\right) \tag{6}$$

$$P4 = p(B2_D|A) = \prod \Phi\left(\frac{lnx - \mu_{D2}}{\beta}\right) - \Phi\left(\frac{lnx - \mu_{D4}}{\beta}\right) \tag{7}$$

$$P5 = p(B2_C|A) = \prod \Phi\left(\frac{lnx - \mu_{D4}}{\beta}\right) \tag{8}$$

where x = specified PGA value for individual chimney
μ = Natural Log value of fragility curve median with subscript denoting damage state
β = beta value in fragility curve analysis
Φ is the standard normal CDF operator
$B2 = \{set\ of\ collapsed\ chimneys\ that\ can\ be\ modeled\ by\ Fragility\ Model\ 2\ (M2)\}$
$B2_C = \{subset\ of\ chimneys\ from\ B2\ that\ collapsed\}$
$B2_{NC} = \{subset\ of\ chimneys\ from\ B2\ that\ did\ not\ collapse\}$
$B2_D = \{subset\ of\ chimneys\ from\ B2\ that\ were\ damaged\}$

To account for the three different P(B|A) equations for the chimney damage states and therefore the probability of observed for M2 ($P_{observed(M2)}$), the P(B|A) for a given GMM is equal to the product of three equations. This can be expressed as follows:

Table 5. Damage states and respective equations

Damage state	No damage	Some damage	Collapse
D-Level	D2	D2–D4	D5
Equation	P3(B_{NC}|A)	P4(B_D|A)	P5(B_C|A)

$$P_{observed(M2)} = P(B2|A) = P3 \cdot P4 \cdot P5 \tag{9}$$

This is completed for each GMM and provides a P(B|A) for both fragility curve methods.

Calculation of P(B). P(B) is calculated from the sum of all P(B|A) values produced by all GMMs for each fragility curve model (Models 1 and 2). This results in an analysis that has two P(B|A) values determinant on the respective fragility curve model:

$$P(Bx) = \sum_{i=1}^{N_{GMM\ Models}} P(Bx|A_i)P(A_i) \tag{10}$$

$$M1 = x = 1; M2 = x = 2$$

P(A) determination. The analysis considers two iterations of priors. The first iteration assumes equal probability of GMM prior distributions. The GMM weights therefore reflect the likelihood of the respective GMMs based on only the Woods Point earthquake analysis (forthwith "uniform prior"). The second iteration takes the prior distribution from GMM logic tree weights determined from expert elicitation for NSHA18 (forthwith "NSHA18 prior"). The output of the NSHA18 prior model thus reflects an updated NSHA18 GMM weighting.

V_{S30} consideration. The above process was repeated using five different V_{S30} parameters in the GMMs: 270, 400, 560, 760, and 1100 m/s. Multiple shear-wave velocities were considered and included in this study instead of a singular velocity due to not knowing the V_{S30} at each chimney site. We therefore assume uniform V_{S30} site conditions at the location of each chimney. To capture some of this uncertainty, the GMMs were adjusted using model-specific amplification factors based on varying V_{S30} values. Some GMMs do not have amplification factors for varying V_{S30}. In these cases, ground motions calibrated to a reference V_{S30} were adjusted using factors from other published studies. The amplification factors from Seyhan and Stewart (2014) were applied to A12 and SEA09NC. The NGA-East model was adjusted from the reference site condition of 3000 m/s using linear and nonlinear components of the amplification model developed by Stewart et al. (2020) and Hashash et al. (2020), respectively. The Stewart et al. (2020) model weights linear amplification contributions with large impedance contrasts relative to those with relatively gradual velocity gradients. Given typical site conditions for eastern Australian sites are more likely to possess more gradual velocity gradients (e.g. Collins et al., 2003), the full weight is placed on the gradual velocity gradient component of the Stewart et al. (2020) linear amplification model for adjusting the NGA-East model.

Integration of methods into a single P(A|B) value per GMM. The Bayesian analysis calculates a P(A|B) for each of the two fragility curve models within the three Bayesian models (NSHA18 GMMs using uniform priors, NSHA18 GMMs using NSHA18 priors, and all GMMs using uniform priors). One source of epistemic uncertainty is associated with the performance of each fragility curve model and whether one model is more probable to accurately define the fragility of the sampled chimneys. This analysis assumes the fragility curve models are equally probable for four reasons: (1) chimney fragility curves are highly uncertain and there is insufficient information for a hierarchical analysis of both GMMs and fragility curves, (2) multiple chimneys could not be modeled by Model 1 and therefore result in a sample size discrepancy, (3) Model 2 is penalized for aiming to model chimney fragility damage at a higher resolution due to this fragility curve model having five damage states rather than only modeling collapse (Model 1), and (4) the Bayesian analysis is intended to evaluate GMMs and not chimney fragility curves. We hence average the P(A|B) value for both fragility curve methods for their respective GMM within each Bayesian model and therefore assume each chimney fragility model is equal.

Results

Bayesian inference of GMMs

Three Bayesian models were used to evaluate relative GMM model performance for ground motions produced by the Woods Point earthquake using damage to chimneys within the epicentral region. Results of the Bayesian analysis can be seen in Table 6 and can be visualized in Figure 11. The first two models (column 3 and 4 in Table 6; Figure 11a and b), isolate and evaluate only NSHA18 GMMs, the first using uniform priors, and the second using NSHA18 priors. The third model (column 5 in Table 6; Figure 11c) uses all GMMs mentioned in this study with uniform priors.

Results and discussion

At the V_{S30} values considered in this study, and considering only uniform priors, GMMs can be generally grouped by relative performance in the Woods Point earthquake. GMMs used in the NSHA18 for southeast Australia (A12, AB06, BEA14, CY08, CY14, and SEA09NC) perform relatively well compared with the other analyzed GMMs not used in NSHA18 (NGA-E, GEA90SEA, GEA90WA, SEA09YC) (Figure 11). This observation independently supports the selection of GMMs for NSHA18 (Griffin et al., 2018).

Based on the predominance of sedimentary bedrock in the study area, and on the topographic slope as reflected in the seismic site condition map for Australia (McPherson, 2017; Wald and Allen, 2007), the most likely representative site class for the study region is B to B/C (V_{S30} of 760–1100 m/s). In this V_{S30} range, A12, AB06, and CY08SWISS are the best performing GMMs, both with uniform and NSHA18 Bayesian priors (Figure 11, Table 6). However, several of the chimney sites are on alluvial flood plains of Quaternary gravel (e.g. Licola, Jamieson) or on sloped sites (e.g. Woods Point). These spatial variations are predominantly smaller than the spatial resolution used to determine V_{S30} pixel values for the site class condition map. The thickness of low-velocity unconsolidated sediments at each site is unknown (probably <5–10 m, but not measured) and the potential effect of slope on site amplification is an additional epistemic uncertainty. To partially address this uncertainty, we also considered relative performance of GMMs at lower V_{S30} values (270–560 m/s). CY08SWISS, CY14, and AB06 are the best performing GMMs in

Table 6. Bayesian analysis results of NSHA18 GMMs and All GMMs assuming fragility curves are equally likely to be correct

Velocity (m/s)	GMM	NSHA18 GMMs – averaged likelihood – uniform prior	NSHA18 GMMs – averaged likelihood – NSHA18 priors	All GMMs – averaged likelihood
270	A12	0.005	0.007	0.005
	AB06	0.146	0.135	0.142
	BEA14	0.073	0.082	0.071
	CY08	0.600	0.604	0.584
	CY14	0.134	0.117	0.131
	SEA09NC	0.040	0.055	0.039
	Gea90SEA			0.013
	Gea90WA			0.014
	SEA09YC			0.000
	NGA-E			0.000
400	A12	0.012	0.016	0.011
	AB06	0.200	0.182	0.196
	BEA14	0.093	0.102	0.091
	CY08	0.480	0.486	0.469
	CY14	0.159	0.136	0.156
	SEA09NC	0.058	0.078	0.057
	Gea90SEA			0.008
	Gea90WA			0.012
	SEA09YC			0.000
	NGA-E			0.000
560	A12	0.048	0.063	0.047
	AB06	0.249	0.222	0.243
	BEA14	0.118	0.128	0.136
	CY08	0.312	0.317	0.262
	CY14	0.199	0.169	0.213
	SEA09NC	0.076	0.100	0.085
	Gea90SEA			0.007
	Gea90WA			0.006
	SEA09YC			0.000
	NGA-E			0.000
760	A12	0.151	0.189	0.149
	AB06	0.262	0.224	0.258
	BEA14	0.112	0.118	0.110
	CY08	0.193	0.188	0.191
	CY14	0.180	0.149	0.179
	SEA09NC	0.102	0.132	0.101
	Gea90SEA			0.007
	Gea90WA			0.004
	SEA09YC			0.000
	NGA-E			0.000
1100	A12	0.340	0.412	0.324
	AB06	0.269	0.222	0.260
	BEA14	0.019	0.020	0.019
	CY08	0.271	0.249	0.263
	CY14	0.061	0.049	0.060
	SEA09NC	0.039	0.048	0.038
	Gea90SEA			0.009
	Gea90WA			0.006
	SEA09YC			0.021
	NGA-E			0.000

GMM: ground motion model.

Results display three Bayesian analyses, one incorporating the NSHA18 expert elicitations (NSHA18 priors), one with uniform priors, and one with all GMMs using uniform priors. Averaged likelihood represents P(A|B).

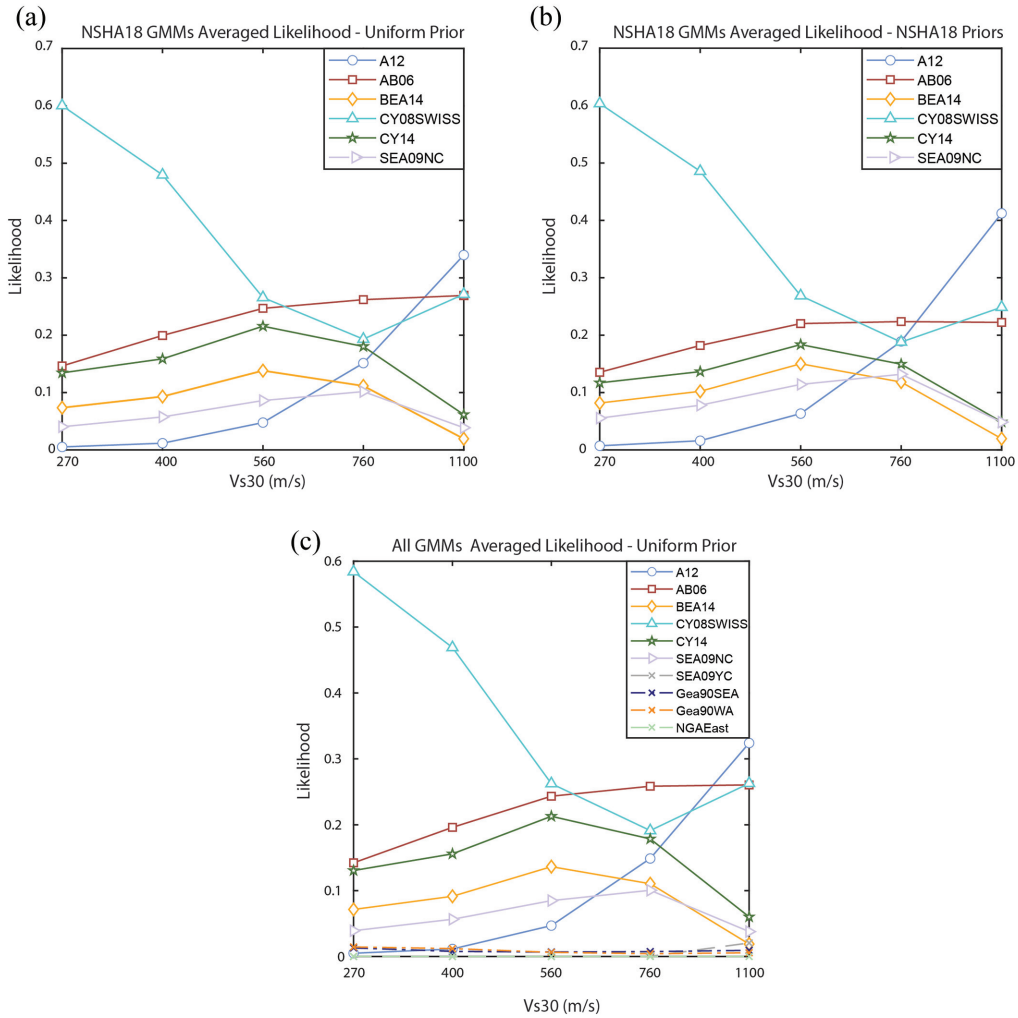

Figure 11. Results of Bayesian GMM likelihoods at all velocities assuming fragility curves are equally likely to be correct. The results display three Bayesian analyses, one incorporating the NSHA18 expert elicitations (priors: 11b) and one without (Uniform Prior/no prior: 11a and one considering all GMMs with no priors (11c). The likelihood is the P(A|B) for each GMM. (a) NSHA18 GMMs averaged likelihood—uniform prior. (b) NSHA18 GMMs averaged likelihood—NSHA18 priors. (c) All GMMs averaged likelihood—uniform prior.

this V_{S30} range with uniform and NSHA18 priors (Figure 11, Table 6). Further study could include estimation of V_{S30} at each individual site and consideration of nonuniform V_{S30} parameters within a single model; we acknowledge the simplification of uniform V_{S30} parameters within individual models as a limitation of our study.

A comparison of NSHA18 GMM performance in the Woods Point earthquake (uniform priors) with the pre-earthquake NSHA18 GMM weightings (NSHA18 priors) is useful to consider how the outputs of the Bayesian approach (which could inform GMM weightings in future NSHAs) relate to the NSHA18 weightings (Table 7). The percent

Table 7. Results of NSHA18 GMMs uniform prior and NSHA18 priors

Velocity (m/s)	GMM	NSHA18 GMMs – averaged likelihood – uniform prior	NSHA18 weighting	NSHA18 GMMs – averaged likelihood – NSHA18 Prior	Percent residual (%)
760	A12	0.151	0.208	0.189	−9.1
	AB06	0.262	0.138	0.224	62.0
	BEA14	0.112	0.166	0.118	−28.8
	CY08SWISS	0.193	0.153	0.188	22.8
	CY14	0.180	0.13	0.149	14.9
	SEA09NC	0.102	0.205	0.132	−35.7
1100	A12	0.340	0.208	0.412	98.2
	AB06	0.269	0.138	0.222	61.0
	BEA14	0.019	0.166	0.020	−88.2
	CYO8SWISS	0.271	0.153	0.249	62.6
	CY14	0.061	0.13	0.049	−62.5
	SEA09NC	0.039	0.205	0.048	−76.4

GMM: ground motion model.
Percent residual refers to percentage difference between the NSHA18 weighting and the results from the Bayesian approach to evaluating NSHA18 GMMs using NSHA18 priors. A positive percent residual refers to the Bayesian analysis resulting in a higher weight for the GMM with the negative residual referencing a reduced weighting for the GMM from the Bayesian analysis.

residual is a metric for this difference; a positive residual reflects an increase in the relative performance (weighting) of a GMM through incorporation of the Woods Point performance with the NSHA18 priors, and a negative residual indicates a reduction in relative performance. In the most likely V_{S30} range, some GMM percent residuals are dependent on which V_{S30} value is used (e.g. A12, CY14), while for others, weightings either increase (e.g. AB06, CY08SWISS) or decrease (BEA14, SEA09NC).

There are substantive uncertainties involving the implications of the refined GMM weightings using the Woods Point earthquake (Table 7) to weighting GMMs in future NSHAs. These include (1) the GMM relative performance for the Woods Point earthquake is determined only for this earthquake, and thus the applicability to GMM relative performances in future earthquakes is uncertain; (2) the study is confined to the near-source region, and it is therefore unknown whether the weightings are relevant at distances beyond the near-source; (3) the study sites are not uniformly spatially distributed with respect to the earthquake source and thus could be susceptible to spatial anisotropies in ground motions and associated sampling biases; (4) the faulting kinematics of the Woods Point earthquake are distinct from prior events that informed NSHA18 GMM weightings, and thus diverse faulting mechanisms in future earthquakes could result in different weightings than those presented here; (5) possible spatial variations in V_{S30} among sites are not considered, and thus GMM relative performance rankings could vary if site-to-site V_{S30} variations were applied; and (6) GMM performance is evaluated using non-instrumental proxies and thus translation to specific instrumental measures including PGA and SA is challenging. This issue of using a single event to evaluate GMMs is further complicated by the inter-event variability of Woods Point earthquake. Observed ground motions at different periods may be substantially higher or lower than median predicted ground motions (Baker and Cornell, 2005). GMM—instrument analysis in Figure 2 and Hoult et al. (2021b) suggest that at distances of 50–150 km, the Woods Point earthquake is a positive epsilon event (i.e. has specific period ranges where SAs exceed median spectral

response curves; Baker and Cornell, 2005). If this event is a positive epsilon event, our study would preference GMMs that estimate higher PGAs and ultimately affect the final weightings. A comprehensive approach would be to repeat this analysis over multiple earthquakes, as randomly chosen events should ultimately aggregate to an epsilon averaging zero (Baker and Cornell, 2005). A final uncertainty is the fragility curves themselves. Different methodologies, chimney parameter inputs (e.g. masonry tensile strength), and beta values will impact the results and interpretations of this study.

Acknowledging these uncertainties, consideration could be given to down-weighting GMMs that under-performed in the Woods Point earthquake and increasing the relative weights of GMMs with increased performance for future NSHAs; however, we do not suggest that absolute weights assigned in any future GMM logic trees should adhere resolutely to the Bayesian output weightings in Table 7. Given the epistemic uncertainties, aleatoric variability, and potential for sampling biases, we cannot advocate for exclusion of any of the NSHA18 GMMs or NGA-East from consideration in future NSHAs on the basis of their relative performance in the Woods Point earthquake alone.

In terms of specific GMM performance, A12, AB06, and CY08SWISS are the GMMs that best match the chimney damage observations. At low V_{S30} values (270 and 400 m/s), the clear statistical preference is CY08SWISS, presumably because V_{S30} scaling in other GMMs overestimated PGA relative to the PGA inferred from observations of chimney damage. This is attributed to CY08SWISS predicting relatively low PGAs at low V_{S30s}. At high V_{S30s}, A12 is the best performing GMM. The A12 model is curated for southeastern Australia and uses a stochastic finite-fault simulation technique (e.g. Motazedian and Atkinson, 2005) involving the use of reinterpreted source and attenuation parameters for small to moderate magnitude southeast Australian earthquakes. Similarly, the AB06 GMM uses a stochastic finite-fault simulation technique using earthquakes from the ENA region. A12 and AB06 models are both considered to perform well due to similar simulation techniques and the use of similar geometrical attenuation coefficients in the near-source region (Allen, 2012; Allen and Atkinson, 2007; Atkinson, 2004; Hoult et al., 2021a). Allen and Atkinson (2007) concluded that there is no significant difference in source characteristics of ENA and SEA earthquakes. This was used for justification of the inclusion of AB06 in the NSHA18 GMM suite. CY08SWISS also performed well. The CY08SWISS model was adjusted for use within the 2015 Swiss Seismic Hazard map (Edwards et al., 2016) and this variation of the model has been used here. The geology of deformed and thrusted Mesozoic sediment overlying crystalline basement in Switzerland (Pfiffner, 2021) is crudely geologically analogous with the deformed Silurian to early Middle Devonian Victorian Highlands of Australia (Fergusson et al., 1986) and thus, similarities in seismic attenuation characteristics between the two regions could be expected. The SEA09NC model performs relatively poorly compared with other NSHA18 models across the range of V_{S30}, but outperforms non-NSHA18 models at all V_{S30} values excluding 1100 m/s (Figure 11). If the performance in the Woods Point earthquake is borne out in other earthquakes, future consideration of NSHA logic tree weightings could consider downweighing or exclusion of the SEA09NC model for this part of Australia. The Yilgarn craton (SEA09YC) version of this GMM performs poorly and on average predicts the second highest expected PGA behind NGA-East, which should have resulted in more chimney failure. The CY14 and BEA14 models represent the California region of the Western US. These models perform relatively well in the 560–760 m/s velocity range. However, the performance of these models—particularly BEA14—decreases at the 1100 m/s range. The CY14 model uses $Z_{1.0}$ and $Z_{2.5}$ inputs intended to model basin effects. However, these

variables were not measured at each chimney site. Rather, standard generic proxies are used. This omits $Z_{1.0}$ and $Z_{2.5}$ as contributing factors into the increased likelihood of this model within low velocity ranges (400 m/s). This highlights CY14 as a well-performing GMM without consideration of basin effects. The Gaull et al. (1990) models (SEA and WA) both performed poorly. These models were not included in NSHA18 due to poor model performance against ground motion records and challenges with the conversion of local magnitude to moment magnitude. Their poor performance in the Woods Point earthquake further justifies their exclusion from future NSHAs. The NGA-East model is the among the worst performing models for the near-source region. We find that NGA-East likely overestimates ground motions within the epicentral region for the Woods Point earthquake.

Considering all of these aspects, one hypothesis that we are continuing to test is that ground accelerations in the near-field region of the Woods Point earthquake in the frequency range relevant to chimney damage were lower than anticipated relative to "median" ground accelerations for an earthquake of this magnitude. Other environmental features may shed light on this hypothesis (La Greca and Quigley, 2021; Quigley and La Greca, 2021).

Conclusion

We developed a Bayesian approach to evaluate the relative performance of GMMs in the near-source (0–50 km) region of the moderate magnitude (5.9 M_W) intraplate 2021 Woods Point earthquake using independent observations of chimney damage and chimney fragility curves. For each chimney, the probability of a given GMM producing PGAs consistent with chimney damage states was calculated across a range of V_{S30} values. At the most likely V_{S30} (760 m/s), the best performing models are AB06, A12, and CY08SWISS. GMMs that were preferentially selected for utility in the Australian National Seismic Hazard Model (NSHA18) prior to the Woods Point earthquake outperform other GMMs, providing additional, independent support for their selection. The recently developed NGA-East GMM performs relatively well in the more distal region (e.g. >50 km) but is among the poorest performing GMMs in the near-source region across the range of V_{S30}. This could reflect unsuitability of the V_{S30}—adjusted NGA-East GMM relative to other GMMs to predict near-field ground motions for the Woods Point earthquake and possibly other earthquakes in southeast Australia. Further study of the parameters and uncertainties in NGA-East GMMs and site amplification models may provide further insights into this observation. Alternatively (or in addition), the relative performance of GMMs could reflect epistemic uncertainties in our proxy approach (e.g. methodological deficiencies and/or parametric uncertainties in using chimneys to estimate ground motions). A final consideration is that ground accelerations in the near-field region of the Woods Point earthquake in the frequency range relevant to chimney damage were lower than anticipated relative to "median" ground accelerations for an earthquake of this magnitude. The Woods Point earthquake is the largest instrumentally recorded earthquake in this region and the first moderate magnitude ($M_W > 5$) strike-slip earthquake in Australia; as such it provides valuable information to enrich the seismic catalog and consider the relative performance of GMMs in predicting ground shaking intensity distributions here and analogous regions globally.

Acknowledgments

We want to thank the Seismology Research Centre for sharing their seismic data, which greatly contributed to this study. We're also grateful to AuScope (www.auscope.org.au) for providing funding for earthquake reconnaissance that allowed us to collect the data used in this manuscript.

Declaration of conflicting interests

The author(s) declared no potential conflicts of interest with respect to the research, authorship, and/or publication of this article.

Funding

The author(s) received no financial support for the research, authorship, and/or publication of this article.

ORCID iDs

James La Greca https://orcid.org/0000-0002-5834-3597
Trevor Allen https://orcid.org/0000-0003-3420-547X

Supplemental material

Supplemental material for this article is available online.

References

Allen T (2012) *Stochastic Ground-motion Prediction Equations for southeastern Australian Earthquakes using Updated Source and Attenuation Parameters* (Record 2012/69). Canberra, ACT, Australia: Geoscience Australia.

Allen T, Carapetis A, Bathgate J, Ghasemi H, Pejić T and Moseley A (2019) Real-time community internet intensity maps and ShakeMaps for Australian earthquakes. In: *Australian Earthquake Engineering Society 2019 conference*, Newcastle, NSW, 29 November–1 December. Available at: https://aees.org.au/wp-content/uploads/2019/12/29-Trevor-Allen.pdf

Allen T, Griffin J and Clark D (2018) *The 2018 National Seismic Hazard Assessment for Australia: Model Input Files* (Record 2018/032). Canberra, ACT, Australia: Geoscience Australia.

Allen TI and Atkinson GM (2007) Comparison of earthquake source spectra and attenuation in eastern North America and southeastern Australia. *Bulletin of the Seismological Society of America* 97(4): 1350–1354.

Allen TI, Cummins PR, Dhu T and Schneider JF (2007) Attenuation of ground-motion spectral amplitudes in southeastern Australia. *Bulletin of the Seismological Society of America* 97: 1279–1292.

Allen TI, Ghasemi H and Griffin JD (2023) Exploring Australian hazard map exceedance using an Atlas of historical ShakeMaps. *Earthquake Spectra* 39: 985–1006.

Allen TI, Wald DJ and Worden CB (2012) Intensity attenuation for active crustal regions. *Journal of Seismology* 16: 409–433.

Atkinson GM (2004) Empirical attenuation of ground-motion spectral amplitudes in southeastern Canada and the northeastern United States. *Bulletin of the Seismological Society of America* 94: 1079–1095.

Atkinson GM and Boore DM (2006.) Earthquake ground-motion prediction equations for eastern North America. *Bulletin of the Seismological Society of America* 96(6): 2181–2205.

Atkinson GM, Worden CD and Wald DJ (2014) Intensity prediction equations for North America. *Bulletin of the Seismological Society of America* 104: 3084–3093.

Baker JW and Cornell CA (2005) A vector-valued ground motion intensity measure consisting of spectral acceleration and epsilon. *Earthquake Engineering and Structural Dynamics* 34(10): 1193–1217.

Bayes T (1764) An essay toward solving a problem in the doctrine of chances. *Philosophical Transactions of the Royal Society of London* 53: 370–418.

Bommer JJ, Douglas J, Scherbaum F, Cotton F, Bungum H and Fäh D (2010) On the selection of ground-motion prediction equations for seismic hazard analysis. *Seismological Research Letters* 81(5): 783–793.

Boore DM, Stewart JP, Seyhan E and Atkinson GM (2014) NGA-West2 equations for predicting PGA, PGV, and 5% damped PSA for shallow crustal earthquakes. *Earthquake Spectra* 30(3): 1057–1085.

Chiou BSJ and Youngs RR (2014) Update of the Chiou and Youngs NGA model for the average horizontal component of peak ground motion and response spectra. *Earthquake Spectra* 30(3): 1117–1153.

Collins CDN, Drummond BJ and Nicoll MG (2003) Crustal thickness patterns in the Australian continent. In: Hillis RR and Müller RD (eds) *Evolution and Dynamics of the Australian Plate*, vol. 372. Boulder, CO: Geological Society of America, pp. 121–128.

Edwards B, Cauzzi C, Danciu L and Fäh D (2016) Region-specific assessment, adjustment, and weighting of ground-motion prediction models: Application to the 2015 Swiss seismichazard maps. *Bulletin of the Seismological Society of America* 106(4): 1840–1857.

Federal Emergency Management Agency (FEMA) (2018) *Seismic performance assessment of buildings volume 1 —Implementation guide*. Technical report, FEMA P-58-1. Washington, DC: FEMA.

Fergusson CL, Gray DR and Cas RA (1986) Overthrust terranes in the Lachlan Fold Belt, southeastern Australia. *Geology* 14(6): 519–522.

Gaull BA, Michael-Leiba MO and Rynn JMW (1990) Probabilistic earthquake risk maps of Australia. *Australian Journal of Earth Sciences* 37(2): 169–187.

Ghasemi H and Allen T (2018) *Selection and Ranking of Ground-Motion Models for the 2018 National Seismic Hazard Assessment of Australia: Summary of Ground-Motion Data, Methodology and Outcomes* (Record 2018/029). Canberra, ACT, Australia: Geoscience Australia.

Goulet CA, Bozorgnia Y, Kuehn N, Al Atik L, Youngs RR, Graves RW and Atkinson GM (2017) *NGA-East ground-motion models for the U.S. Geological Survey National Seismic Hazard Maps*. Pacific Earthquake Engineering Research Center PEER Report No. 2017/03. Berkeley, CA: Pacific Earthquake Engineering Research Center.

Goulet CA, Bozorgnia Y, Kuehn N, Al Atik L, Youngs RR, Graves RW and Atkinson GM (2021) NGA-East ground-motion characterization model part I: Summary of products and model development. *Earthquake Spectra* 37(Suppl. 1): 1231–1282.

Griffin JD, Allen TI and Gerstenberger MC (2020) Seismic hazard assessment in Australia: Can structured expert elicitation achieve consensus in the "land of the fair go"? *Seismological Research Letters* 91: 859–873.

Griffin JD, Gerstenberger M, Allen T, Clark D, Cuthbertson R, Dimos A, Gibson G, Ghasemi H, Hoult R, Lam N, Leonard M, Mote T, Quigley M, Somerville P, Sinadinovski C, Stirling M and Venkatesan S (2018) *Expert Elicitation of Model Parameters for the 2018 National Seismic Hazard Assessment—Summary of Workshop, Methodology and Outcomes* (Record 2018/028). Canberra, ACT, Australia: Geoscience Australia.

Hashash YMA, Ilhan O, Harmon JA, Parker GA, Stewart JP, Rathje EM, Campbell KW and Silva WJ (2020) Nonlinear site amplification model for ergodic seismic hazard analysis in Central and Eastern North America. *Earthquake Spectra* 36: 69–86.

Heresi P and Miranda E (2021) Fragility curves and methodology for estimating post earthquake occupancy of wood-frame single-family houses on a regional scale. *Journal of Structural Engineering* 147(5): 04021039.

Hoult RD, Allen T, Borleis E, Peck W and Amirsardari A (2021a) Source and attenuation properties of the 2012 Moe, southeastern Australia, earthquake sequence. *Seismological Research Letters* 92(2A): 1112–1128.

Hoult RD, Pascale A, Jones A and Allen T (2021b) The M_W 5.9 Woods Point earthquake: a preliminary investigation of the ground motion observations. In: *Australian Earthquake Engineering Society 2021*, virtual conference, 25–26 November.

Joyce J (2003) Bayes' theorem. In: Zalta EN (ed.) *Stanford Encyclopedia of Philosophy*. Stanford, CA: Stanford University. Available at: https://plato.stanford.edu/archives/fall2021/entries/bayes-theorem/ (accessed March 2022)

Klopp GM (1996) *Seismic design of unreinforced masonry structure*, Dissertation Adelaide: The University of Adelaide.

Krawinkler H, Osteraas JD, McDonald BM and Hunt JP (2012) Development of damage fragility functions for URM chimneys and parapets. In: *15th World conference in earthquake engineering*, Lisbon, 24–28 September.

La Greca J and Quigley M (2021) *Survey of Environmental and Infrastructure Damage From the September 2021 Mw 5.9 Woods Point Earthquake, Victoria, Australia: Part 2* (Earthquake Engineering Research Institute—Australian Earthquake Engineering Society—New Zealand Society of Earthquake Engineering Joint Learning from Earthquakes Clearinghouse: Woods Point, Australia Earthquake, 64 p). Oakland, CA: Earthquake Engineering Research Institute.

Lallemant D, Kiremidjian A and Burton H (2015) Statistical procedures for developing earthquake damage fragility curves. *Earthquake Engineering and Structural Dynamics* 44(9): 1373–1389.

Leonard M (2015) Consistent MMI area estimation for Australian earthquakes. In: *10th Pacific conference on earthquake engineering*, Sydney, NSW, Australia, 6–8 November, Paper 170.

Leonard M, Burbidge DR, Allen TI, Robinson DJ, McPherson A, Clark D and Collins CDN (2014) The challenges of probabilistic seismic-hazard assessment in stable continental interiors: An Australian example. *Bulletin of the Seismological Society of America* 104(6): 3008–3028.

McCue K (2015) *Historical Earthquakes in Victoria: A Revised List*. Richmond, VIC, Australia: Australian Earthquake Engineering Society.

McPherson AA (2017) *A Revised Seismic Site Conditions Map for Australia* (Record 2017/012). Canberra. http://dx.doi.org/10.11636/Record.2017.012

Maison B and McDonald B (2018) Fragility curves for residential masonry chimneys. *Earthquake Spectra* 34(3): 1001–1023.

Moon L, Dizhur D, Senaldi I, Derakhshan H, Griffith M, Magenes G and Ingham J (2014.) The demise of the URM building stock in Christchurch during the 2010–2011 Canterbury earthquake sequence. *Earthquake Spectra* 30(1): 253–276.

Motazedian D and Atkinson GM (2005) Stochastic finite-fault modeling based on a dynamic corner frequency. *Bulletin of the Seismological Society of America* 95: 995–1010.

Mousavi S, Hejrani B, Miller MS and Salmon M (2023) Hypocenter, fault plane, and rupture characterization of Australian earthquakes: Application to the September 2021 MW 5.9 Woods Point earthquake. *Seismological Research Letters* 94: 1761–1774.

Pagani M, Monelli D, Weatherill G, Danciu L, Crowley H, Silva V, Henshaw P, Butler R, Nastasi M, Panzeri L, Simionato M and Vigano D (2014) OpenQuake Engine: An open hazard (and risk) software for the Global Earthquake Model. *Seismological Research Letters* 85: 692–702.

Pfiffner OA (2021) The geology of Switzerland. In: Reynard E (ed.) *Landscapes and Landforms of Switzerland*. Cham: Springer, pp. 7–30.

Quigley M and La Greca J (2021) *Reconnaissance Survey of Environmental and Infrastructure Damage From the September 2021 Mw 5.9 Woods Point Earthquake, Victoria, Australia* (Earthquake Engineering Research Institute—Australian Earthquake Engineering Society—New Zealand Society of Earthquake Engineering Joint Learning from Earthquakes Clearinghouse: Woods Point, Australia Earthquake, 31 p). Oakland, CA: Earthquake Engineering Research Institute.

Quigley M, Pascale A, Clark D and Allen T (2021) Wednesday 22 September 2021 Mw 5.9 Woods Point earthquake—Information sheet. Available at: http://learningfromearthquakes.org/2021-09-22-australia/images/2021_09_22-australia/pdfs/REPORT_EQ_27_SEPT_2021_short.TA.pdf

Ramos-Sepulveda ME, Parker GA, Li M, Ilhan O, Hashash Y, Rathje EM and Stewart J (2022) Performance of NGA-East GMMs and site amplification models relative to CENA ground

motions. In: *12th National conference on earthquake engineering*, Salt Lake City, UT, 27 June–1 July.

Standards Australia (2018). AS1170.4-2007(R2018) Structural design actions Part 4: Earthquake actions in Australia, SA, Sydney, NSW.

Seyhan E and Stewart JP (2014) Semi-empirical nonlinear site amplification from NGA-West 2 data and simulations. *Earthquake Spectra* 30: 1241–1256.

Somerville P, Graves R, Collins N, Song SG, Ni S and Cummins P (2009) Source and ground motion models for Australian earthquakes. In: *Australian Earthquake Engineering Society 2009 Conference*, Newcastle, NSW, Australia, 11–13 December.

Stewart JP, Parker GA, Atkinson GM, Boore DM, Hashash YMA and Silva WJ (2020) Ergodic site amplification model for central and eastern North America. *Earthquake Spectra* 36: 42–68.

Tang Y, Lam N, Tsang H-H and Lumantarna E (2022) An adaptive ground motion prediction equation for use in low-to-moderate seismicity regions. *Journal of Earthquake Engineering* 26: 2567–2598.

Vaculik J and Griffith MC (2017) Out-of-plane load-displacement model for two-way spanning masonry walls. *Engineering Structures* 141: 328–343.

Vaculik J and Griffith MC (2019) Out-of-plane fragility of URM parts and components based on time—history analysis—Comparison to simplified force-based approaches. In: *Australian Earthquake Engineering Society 2019 conference*, Newcastle, NSW, Australia, 29 November–1 December.

Vamvatsikos D and Cornell CA (2002) Incremental dynamic analysis. *Earthquake Engineering and Structural Dynamics* 31(3): 491–514.

Van de Schoot R, Depaoli S, King R, Kramer B, Märtens K, Tadesse MG, Vannucci M, Gelman A, Veen D, Willemsen J and Yau C (2021) Bayesian statistics and modelling. *Nature Reviews Methods Primers* 1: 1.

Wald DJ and Allen TI (2007) Topographic slope as a proxy for seismic site conditions and amplification. *Bulletin of the Seismological Society of America* 97: 1379–1395.

Wald DJ, Jaiswal KS, Marano KD, Bausch DB and Hearne MG (2010) *PAGER—Rapid Assessment of an Earthquake's Impact* (U.S. Geological Survey Fact Sheet 2010–3036, Rev. November 2011). Reston, VA: U.S. Geological Survey.